metals

MDPI

Article

Multi-Physical Field Coupling Analysis of Electro-Controlled Permanent Magnet Blank Holder Processes Considering Thermal Magnetic Losses

Zhanshan Wang [1], Linyuan Meng [2,*], Gaochao Yu [2] and Xiaoyu Ji [3]

[1] Intelligent Equipment Department, Suzhou Vocational Institute of Industrial Technology, Suzhou 215104, China; 00759@siit.edu.cn
[2] School of Mechanical Engineering, Yanshan University, Qinhuangdao 066004, China; ygc@ysu.edu.cn
[3] CCCC Second Harbor Engineering Company Ltd., Wuhan 430040, China; xycccc2024@163.com
* Correspondence: mlyysu@126.com; Tel.: +86-180-3359-0906

Abstract: Electro-permanent magnet (EPM) technology is characterized by high integration, strong modularity, and stable magnetic force, making it a current research focus when combined with sheet metal deep drawing processes to develop EPM blank holder deep drawing technology. In this study, we investigated the issue of thermal magnetic quantitative magnetic loss after the prolonged use of the EPMBH process, analyzing the variation in magnetic force with the temperature increase to provide necessary data support for the application of the EPMBH. First, a thermal network model for the four-magnetic pole unit EPM magnetic device was established, and through calculations on this model, the thermal equilibrium temperatures for the permanent magnet (PM)-NdFeB and reversible magnet (RM)-AlNiCo were found to be 72.13 °C and 72.41 °C, respectively. Second, the magnetic performance of PM and RM at different temperature points was measured to analyze the variation in their magnetic characteristics with the temperature increase. Third, a magnetic force model of the EPM magnetic device was established, and finite element analysis was conducted using the measured magnetic characteristics data of RM and PM. The results indicated that an increase in temperature leads to a reduction in magnetic force, with a maximum reduction of 18.57% observed after thermal equilibrium. An experimental testing platform was designed and built to validate the calculation and simulation results. Finally, a sheet metal deep drawing experiment using the EPMBH process was conducted, taking into account thermal magnetic loss factors. The results showed that magnetic force loss due to temperature rise affects the forming quality of the sheet metal. Therefore, in practical applications, it is necessary to establish a real-time temperature monitoring system and develop a temperature-based magnetic force compensation module.

Keywords: electro-permanent magnet blank holder; deep drawing; temperature-dependent magnetic loss; thermal filed; coupled magnetic–stress field

check for updates

Academic Editor: Mohammad Jahazi

Received: 29 October 2024
Revised: 21 December 2024
Accepted: 30 December 2024
Published: 3 January 2025

Citation: Wang, Z.; Meng, L.; Yu, G.; Ji, X. Multi-Physical Field Coupling Analysis of Electro-Controlled Permanent Magnet Blank Holder Processes Considering Thermal Magnetic Losses. *Metals* **2025**, *15*, 39. https://doi.org/10.3390/met15010039

Copyright: © 2025 by the authors. Licensee MDPI, Basel, Switzerland. This article is an open access article distributed under the terms and conditions of the Creative Commons Attribution (CC BY) license (https://creativecommons.org/licenses/by/4.0/).

1. Introduction

Deep drawing forming is one of the primary methods of sheet metal forming and is widely used in industrial production. During the deep drawing process, if the blank holder force is too low, tangential stress can accumulate in the flange area of the blank, leading to instability and causing the blank to wrinkle [1]; if the blank holder force is too high, it can cause excessive thinning or even fracture at the dangerous edge of the blank.

The application of an appropriate blank holder force is an important means to ensure the quality of the formation [2–4]. Du Bing [5,6] analyzed the loading path and energy flow

direction to establish a critical determination criterion for wrinkling in box-shaped parts. Won [7] analyzed the forming process of box-shaped parts, and the results indicated that the force and deformation distribution in the flange area of the formed parts are uneven. The unreasonable application of blank holder force can easily lead to wrinkling and instability in the flange area, thus affecting product quality and mold life. Susila et al. [8] conducted research on the maximum blank holder force for cup-shaped parts and performed finite element analysis experiments for validation.

Over the past few decades, researchers have conducted in-depth studies on the loading and control modes of blank holder force. Senior [9] and Hill [10] have studied the issue of the critical blank holder force for wrinkling using the energy method and bifurcation theory, respectively. Hauptmann [11] optimized the structure of stretched cardboard by adjusting the relationship between the blank holder force and the stroke in deep drawing. Sim [12], based on the concept of closed-loop control of blank holder force, obtained the curve of blank holder force against stroke for the deep drawing process of cylindrical parts, which can be controlled in real time, using numerical simulation methods. Kergen [13] obtained the ideal blank holder force trajectory curve based on the wrinkle-free experiment that measures the gap between the mold and the blank holder ring. Wang [14] used theoretical calculations and finite element simulation methods to derive the "V" type blank holder force setting mode, which is conducive to reducing the thinning rate of formed parts.

Generally, BHF is applied by hydraulic pressure or other external forces in deep drawing. But, due to high energy consumption, long transmission chains, and complicated control processes during BHF by hydraulic or mechanical transmission, there are some disadvantages in realizing the real-time control of BHF. In order to solve the problems of traditional blank holding, numerous scholars have used auxiliary blank holder devices to load and control the blank holder force, achieving good forming results [15–17]. Seo [18] first proposed the electromagnetic blank holding method. Li [19] developed a new type of electromagnetic blank holder force system suitable for conventional deep drawing processes and verified the effectiveness of the electromagnetic blank holder system. Huang [20] designed a kind of pulsed electromagnetic blank holding system. This method uses the electromagnetic attraction or repulsion generated between coils as the blank holding force acting on the blank holder ring to achieve blank holding. Due to the need for continuous power supply to maintain the magnetic field, there are some difficulties in overcoming defects, such as high energy consumption, coil temperature rise and heating, and safety hazards like demagnetization upon power failure, which limit its further application in actual production.

In the late 20th century, the electro-controlled permanent magnetic chuck was invented by Tecnomagnetes S.P.A. (Lainate, Italy). Afterwards, this technology has been continuously improved and gradually expanded. The electro-controlled permanent magnet technology was originally applied in the fields of lifting, rapid mold changing, and fixing during machining processes [21,22]. The electro-controlled permanent magnet chuck constructed based on this technology has advantages such as independent loading, a short transmission chain, ease of control, and energy efficiency. Qin [23,24] combined the electro-controlled permanent magnet technology with the sheet metal deep drawing process to propose an electro-controlled permanent magnet blank holding method. Tooling and molds were designed based on the magnetic force of electro-controlled permanent magnets for blank holding, and the finite element analysis and experimental verification of the magnetic and stress field were conducted. Qin and Zhang [25,26] have analyzed the temperature rise effect of the EPM in the electro-controlled permanent magnet blank holder (EPMBH) deep drawing process, as well as the thermal field and the magnetic–mechanical field, but they

did not analyze the impact of temperature rise on the magnetic properties of magnetic materials and the magnetic force.

In this paper, we analyze the issue of heat effects generated by the control current passing through the excitation coil in the EPMBH, adopt the thermal network analysis method to establish the thermal transfer network of the magnetic force device of FMPU, and calculate the thermal equilibrium temperature of each component. We also analyze the impact of temperature rise on the magnetic materials in the model, conduct finite element analysis on the coupled fields of temperature, magnetic, and stress fields for FMPUs, and, finally, determine the trend of how temperature rise affects the magnetic force. This provides a basis for force control in the EPMBH deep drawing process to ensure effective and continuous operation.

2. Materials and Methods

2.1. Principle of EPMBH

As shown in Figure 1a, the EPM and the suction plate are the essential components of the EPMBH, together creating a magnetic attraction force. This force serves as the blank holder force necessary for deep drawing operations. A single magnetic pole unit can decompose into three parts: reversible magnet (RM), permanent magnet (PM), and copper coils. Based on the magnetic properties, NdFeB is characterized by high remanence and high coercivity, which allows it to provide strong magnetic force and excellent magnetic stability. AlNiCo is characterized by high remanence and lower coercivity, enabling it to provide strong magnetic force while allowing its magnetic polarity to be changed by an external magnetic field. AlNiCo is selected as the RM, while NdFeB serves as the PM.

The working principle of the EPMBH is highly dependent on the hysteresis property of the AlNiCo. As shown in Figure 1b, AlNiCo demonstrates variable magnetic characteristics under distinct loading currents, manifesting as diverse hysteresis loops. Adjusting the intensity of the loading current allows for the control of the blank holder force, and I_s is the saturation magnetizing current, corresponding to the saturation hysteresis loop of AlNiCo, which produces the maximum blank holder force (BHF) in this state. In the control process, the magnetization direction of NdFeB is fixed; as shown Figure 1b,c, a positive current that induces a magnetic field in the same direction as that of the NdFeB magnet is applied. The state in which the magnetization of the AlNiCo follows the poles of the NdFeB is called the forward state (state (3)). In contrast, the state where the poles of the AlNiCo are the opposite of those of the NdFeB is called a reverse state (state (1)). Figure 1c depicts the full cycle of the EPMBH working principle divided into four steps as follows:

(i) [**Unloading state**]: I (working current) = 0, AlNiCo is in state (1). The magnetic flux lines form a loop within the EPM and do not exhibit magnetic attraction externally.
(ii) [**Forward magnetization state**]: I > 0, loading time is 20 ms, AlNiCo transitions from state (1) through state (2) to state (3)
(iii) [**Loading state**]: I = 0, AlNiCo is in state (3), the magnetic induction lines of the EPM extend outward, exhibiting magnetic attraction, resulting in BHF.
(iv) [**Reverse magnetization state**]: I < 0, loading time is 20 ms, AlNiCo transitions from state (3) through state (4) to state (1).

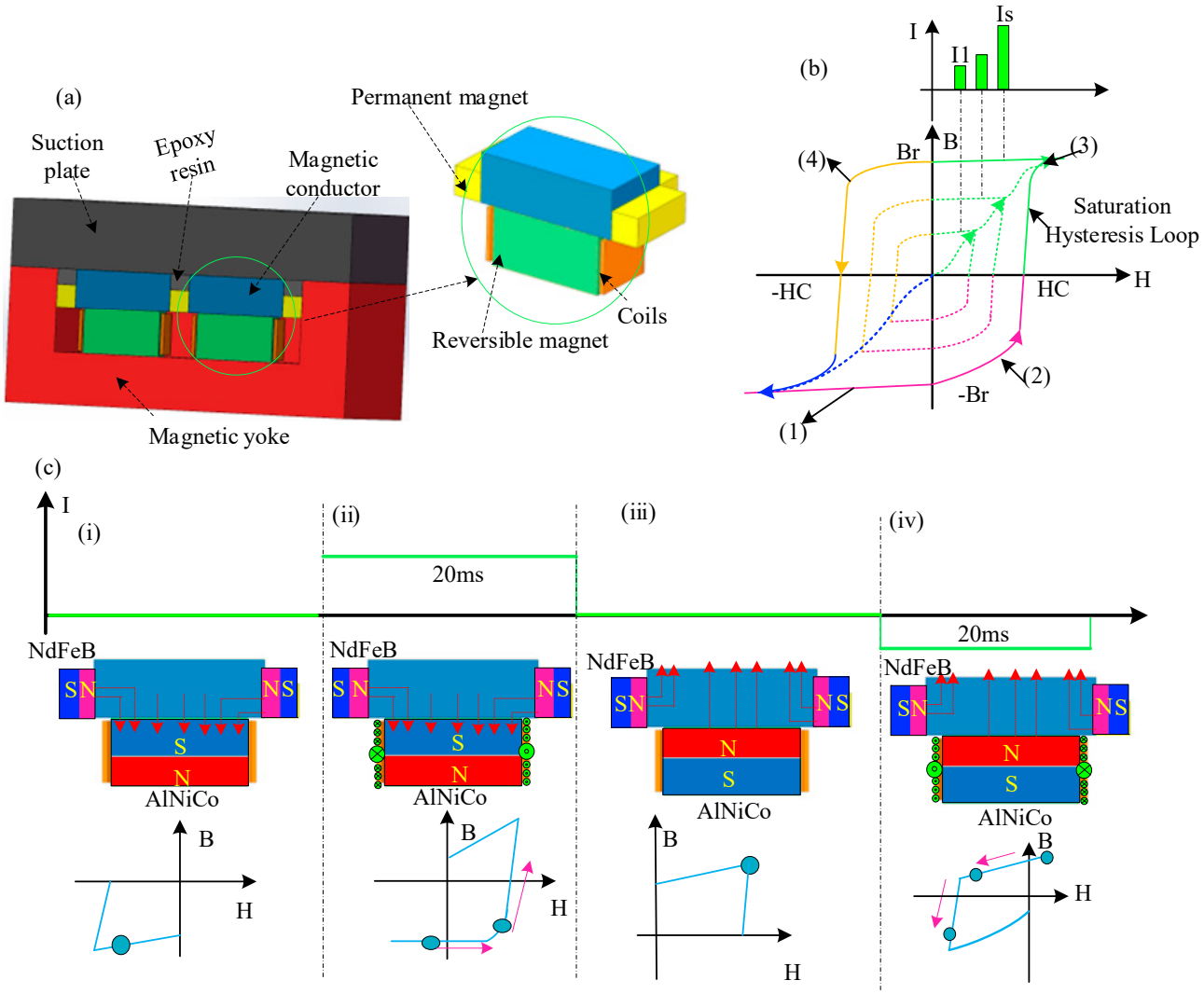


Figure 1. Principle of the EMPBH: (**a**) structure of the EPMBH; (**b**) hysteresis curve of the Al-Ni-Co; (**c**) schematic of the full-cycle fundamental principle of the proposed EPMH; the red arrows represent the magnetic field direction induced inside the core. The blue dots show the estimated field of the EPMBH in the state with an applied current measured at a certain distance from the core tip.

2.2. Setup Tools Using EPMBH

Designing the EPMBH tools, the structure of the EPM magnetic pad is as depicted in Figure 2a, comprising 36 magnet pole units. As shown in Figure 2b, the EPM magnetic pad is integrated with a moveable beam through connecting rods. The sheet metal is positioned between the EPM magnetic pad and the suction plate, which together create a magnetic force; this force is distributed across the slab by a flange ring as BHF to facilitate the deep drawing process. Upon the completion of the deep drawing, the magnet pad is reversed to a demagnetized state, entering an unloading state with no magnetic force between the pad and the suction plate; this allows for the easy removal of the formed part.

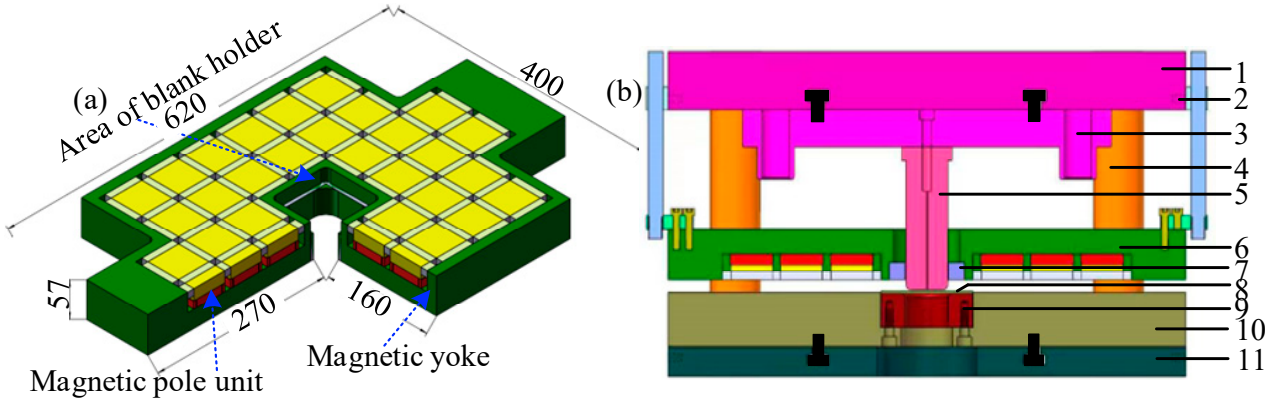


Figure 2. Mold for the EPMBH: (**a**) structure of the EPMBH; (**b**) EPMBH deep drawing tools and 1. movable beam, 2. connecting rod, 3. upper base, 4. guide pillar, 5. punch, 6. EPM, 7. blank holder, 8. sheet metal, 9. die, 10. suction plate, 11. lower base.

2.3. Analyses of Thermal Field of FMPU

2.3.1. Models of FMPU

In EPM technology, the magnetic pole units are used in pairs, and the thermal fields of four magnetic pole units include all the modes of heat conduction in the EPM magnetic pad, so FMPUs are taken as an example for description. As shown in Figure 3a, the dimensions of FMPUs, RMs, and PMs are 150 × 150 × 50 mm, 45 × 45 × 20 mm, and 43 × 43 × 12 mm, respectively. As shown in Figure 3b, resistance temperature detectors (RTDs) are positioned inside the 4-EPM. RTD-1 is located within the coil to assess its temperature, RTD-2 is mounted on the NdFeB surface for tracking its thermal state, and RTD-3 is placed atop the AlNiCo surface to gauge its temperature.

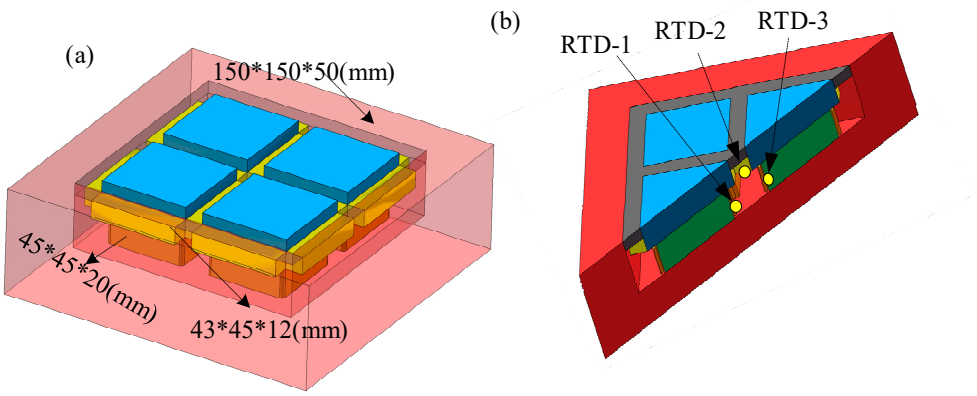


Figure 3. Mold for FMPUs: (**a**) 3D diagram; (**b**) sectional view.

2.3.2. Thermal Network Model for FMPUs

The thermal network model based on thermal resistance and capacitance for FMPUs was established, and the integrated nodes in the thermal network model were numbered. As shown in Figure 4, the numbering situation was as follows: epoxy resin (5, 9, 13, 16), PM (1, 2, 3, 4, 6, 7, 8, 10, 11, 12, 14, 15), RM (18, 20, 22, 24), coil (19, 21, 23, 25), magnetic yoke (17), and air (26).

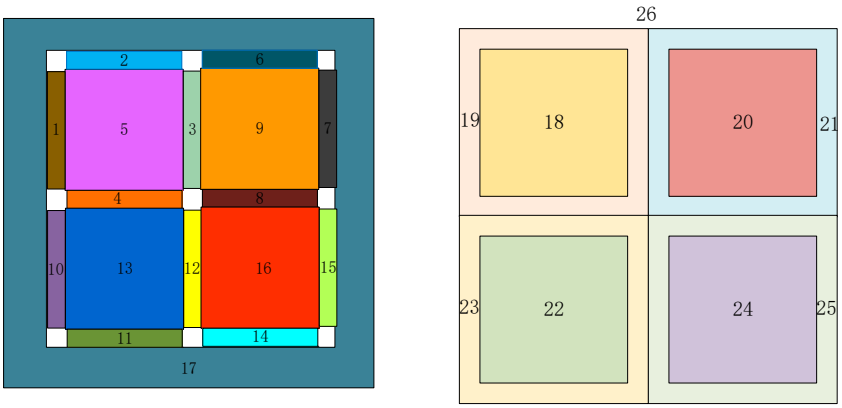


Figure 4. Node number for FMPUs: (**a**) the numbering situation of the surface; (**b**) the numbering situation of the interior.

The thermal network model method was based on thermal resistance, wherein there are mainly three forms of thermal resistance, namely conduction thermal resistance, convection thermal resistance, and radiation thermal resistance, while in the FMPUs, there are mainly conduction thermal resistance and convection thermal resistance. The thermal resistance R*ij* between the parts in the heat transfer network represents the thermal resistance of the number *i* and the number *j*, as shown in Table 1. And the schematic diagram of the thermal network model as shown in Figure 5.

Table 1. Thermal resistance form.

Thermal Resistance Form	Number
conduction thermal resistance	R5.1, R5.2, R5.3, R5.4, R9.6, R9.7, R9.3, R9.8, R13.4, R13.10, R13.12, R13.11, R16.8, R16.12, R16.14, R16.15, R18.5, R20.9, R24.25, R22.13, R24.16
contact thermal resistance	R22.23, R17.1, R17.7, R17.11, R17.20, R17.19, R17.25, R17.2, R17.15, R17.10, R17.22, R17.21, R20.21, R18.19, R17.6, R17.14, R17.18, R17.24, R17.23,
convection thermal resistance	R26.others

According to heat transfer theory, the conductive thermal resistance can be represented in Equation (1).

$$R_{i,j} = \frac{L_i}{2\lambda_i A_{i,j}} + \frac{L_j}{2\lambda_j A_{i,j}} \quad (1)$$

where the $R_{i,j}$ is the thermal resistance of conduction between node i and j (K/W); L_i is the length of the conduction direction at node i (mm); L_j is the length of the conduction direction at node i (mm); λ_i is the thermal conductivity of material i (W/(m·K)); λ_j is the thermal conductivity of material j (W/(m·K)); and $A_{i,j}$ is the conductive area between node i and j (mm^2).

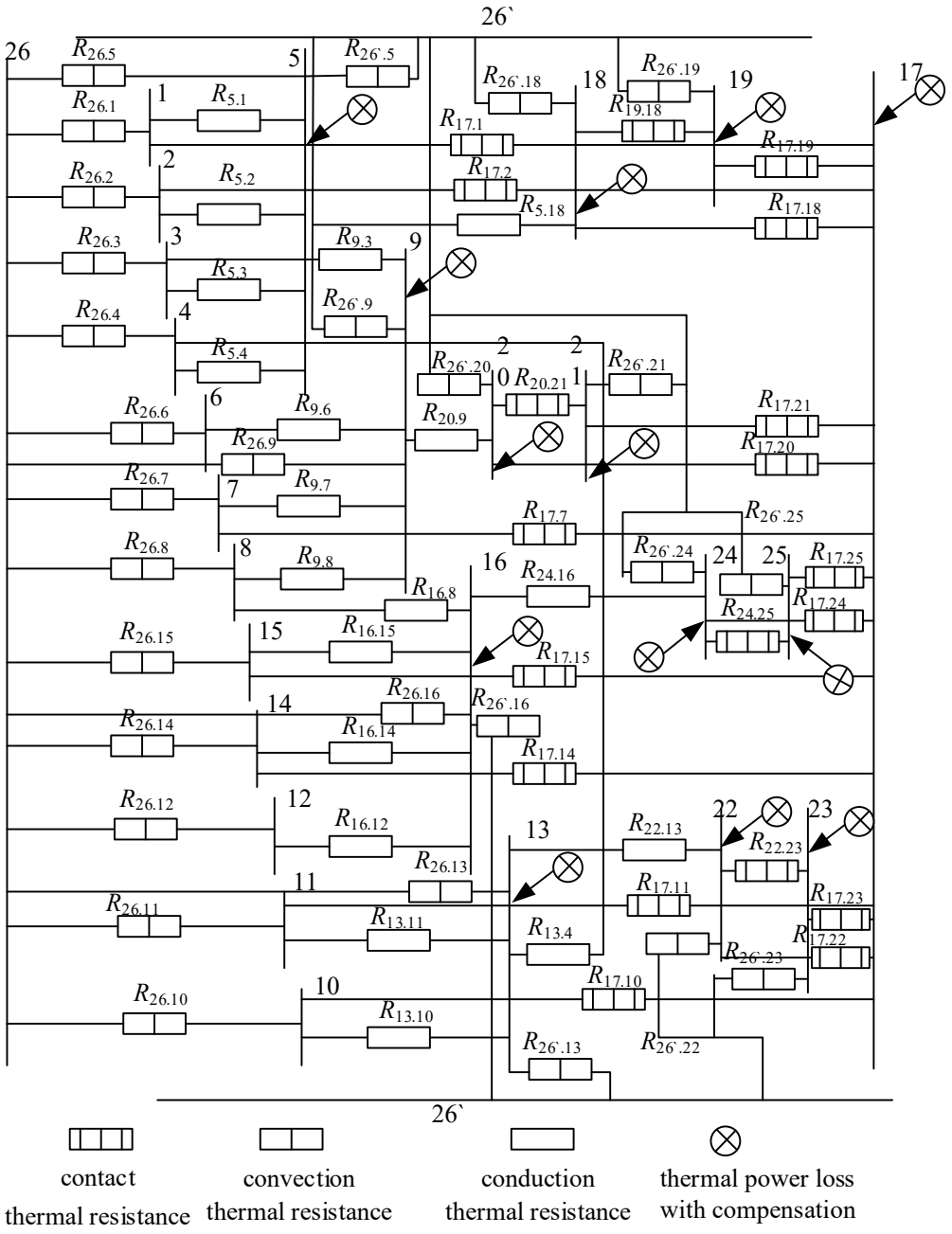


Figure 5. Thermal network model of four-pole chuck with compensation.

Due to the temperature difference between the suction cup component and the external environment, convective heat transfer occurs between the solid and the fluid. The exterior of the suction cup is in direct contact with the air, and the parts in contact with the air are all considered as convective thermal resistance, as can be expressed in Equation (2):

$$R_D = \frac{1}{hA} \tag{2}$$

where R_D is the convective thermal resistance (K/W) and h is the convective heat transfer coefficient (W/(m^2·K)).

Contact thermal resistance exists between two objects with a small contact area. Contact thermal resistance includes both conductive thermal resistance and convective thermal resistance. Because the contact rate of the two parts is relatively low and the proportion of the interspersed air domains is high, the calculation formula is derived by adding the

conductive thermal resistance and convective thermal resistance together, which can be expressed in Equation (3):

$$R_j = \frac{1}{hA_1} + \frac{L}{hA_2} \tag{3}$$

where R_j is the contact thermal resistance (K/W); A_1 is the convective contact area (mm^2); and A_2 is the conduction contact area (mm^2).

Based on the thermal network model of the suction cup, establish the thermal equilibrium equation for each temperature node. According to the heat flow rules within the suction cup, establish the thermal equilibrium equations for all the set temperature nodes through Kirchhoff's law and the law of conservation of energy. All temperature nodes within the suction cup comply with the law of conservation of energy.

$$Q_{in} = \Delta Q + Q_{out} \tag{4}$$

$$Q_{out} = \frac{T_i - T_j}{R_{ij}} + \frac{T_i - T_k}{R_{ik}} \tag{5}$$

$$\Delta Q = \frac{mc\Delta T}{\Delta \tau} \tag{6}$$

$$\sum_k \frac{T_i - T_k}{R_{ki}} + \sum_j \frac{T_i - T_j}{R_{ji}} + m_i c_i \frac{\Delta T_i}{\Delta \tau} = Q_i \tag{7}$$

Upon achieving thermal equilibrium at each node of the FMPUs, 26 temperature balance equations can be formulated as Equation (7). The consolidation of these equations yields the matrix for the thermal equilibrium equations:

$$[R]_{n\times n}[T]_{n\times 1} = [Q]_{n\times 1} \tag{8}$$

where $[R]_{n\times n}$ is the thermal resistance matrix of the nodes; $[T]_{n\times 1}$ is the temperature vector of the nodes; and $[Q]_{n\times 1}$ is the heat source vector of the nodes.

Setting the baseline temperature to 25 °C, the temperature of the nodes can be calculated by inputting the thermal resistance and heat dissipation into the matrix. The uniformity in the external conditions for the nodes of the main permanent magnets—3, 4, 8, and 12, and similarly for nodes 1, 2, 6, 7, 10, 11, 14, and 15—owing to the symmetrical design of the suction cup, results in identical threshold temperatures for these nodes. Consequently, nodes 3, 4, 8, and 12 share the same maximum temperature, as do nodes 1, 2, 6, 7, 10, 11, 14, and 15. Extending this uniformity, pole piece nodes 5, 9, 13, and 16; reversible permanent magnet nodes 18, 20, 22, and 24; and coil nodes 19, 21, 23, and 25 also exhibit equivalent temperatures. The precise temperature readings for these nodes are presented in Table 2.

Table 2. Table of temperature values calculated for each component.

Components of FMPUs	Node Number	T (°C)
PM	3, 4, 8, 12	72.13
Magnetic conductor	5, 9, 13, 16	70.97
Coils	19, 21, 23, 25	74.63
PM	1, 2, 6, 7, 10, 11, 14, 15	71.25
RM	18, 20, 22, 24	72.41
Magnetic yoke:	17	72.52

2.4. Analysis of the Coupling Fields of FMPUs

2.4.1. Magnetic Performance Testing of PM and RM at Different Temperatures

The RM (Alnico) and PM (NdFeB) serve as the fundamental elements of the EPM magnetic chuck, playing a crucial role by supplying the necessary blank holder force in the process of deep drawing form. The magnetic force degradation during temperature rise is primarily due to the thermal-induced magnetic losses in both the PMs and RMs. Temperature analysis was conducted on a 4-pole electro-controlled permanent magnetic chuck model using the network calculation method, which determined that the peak temperatures reached 72.13 °C for NdFeB and 72.41 °C for AlNiCo. Vibrating Sample Magnetometer (VSM) tests were conducted on PM and RM materials at three temperature points, namely 25 °C (ambient temperature), 50 °C, and 75 °C, to assess their magnetic properties, as shown in Figure 6a. The magnetic performance curves of PMs and RMs are shown in Figure 6b,c, and the test data are presented in Table 3.

Table 3. Magnetic property test table of permanent magnet materials at different temperatures.

Material	T (°C)	Br (T)	HcB (KOe)	HcJ (KOe)	(BH)max (MGOe)
AlNiCo	25	1.0942	0.6580	0.6690	3.495
	50	1.0921	0.6605	0.6731	3.515
	75	1.0839	0.6604	0.6726	3.529
NdFeB	25	1.197	10. 51	11.94	32.063
	50	1.1767	9.7062	10.2738	30.839
	75	1.0996	6.5463	6.7787	26.357

Upon analyzing the magnetic characteristic test results, it is observed that for AlNiCo, the maximum fluctuation in residual magnetism (B_r) with an increase in temperature is 0.94%, the coercive force (H_{Cj}) fluctuates up to 0.53%, and the maximum decrease in the magnetic energy product ($(BH)_{max}$) is 0.09%. This demonstrates that AlNiCo's magnetic properties remain stable during a temperature rise. For NdFeB, the residual magnetism (B_r) decreases by 0.0203(T) when the temperature goes from 25 °C to 50 °C, which is a reduction of 1.69%; the coercive force (H_{Cj}) reduces by 0.8038(KOe), a decrease of 7.6%; and the maximum magnetic energy ($(BH)_{max}$) product decreases by 1.224(MGOe). When the temperature reaches 75 °C, the residual magnetism (B_r) further decreases by 0.0974(T), a reduction of 8.14%; the coercive force (H_{Cj}) decreases by 3.9637(KOe), a decrease of 37.71%; and the maximum magnetic energy ($(BH)_{max}$) product (BH)max decreases by 5.706 (MGOe), a reduction of 17.79%. It can be concluded that NdFeB has poor temperature stability and its magnetic properties decline with an increase in temperature. The test results are consistent with the trend observed in previous studies [27], but there are slight differences in the magnitude of change. This is attributed to variations in the manufacturing processes and batch differences.

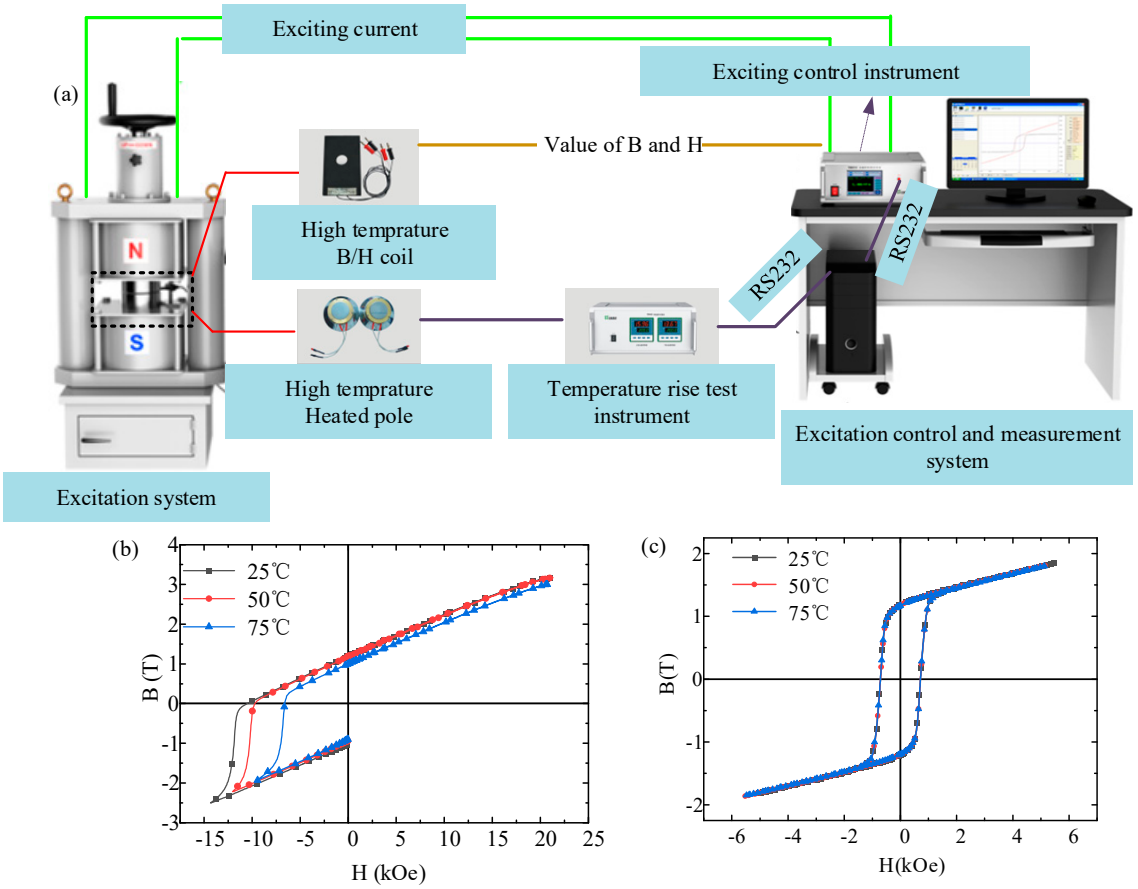


Figure 6. Magnetic property detection of magnetic materials with temperature variation: (**a**) schematic diagram of detection principle; (**b**) magnetic property curves of NdFeB at different temperatures; (**c**) magnetic property curves of AlNiCo at different temperatures.

2.4.2. Analysis of Coupling Fields

In the EPMBH process, the blank holder force derives from the combined magnetic force of the EPM magnetic pad and the magnetic attraction from the suction plate. Throughout this process, the control current remains inactive, leaving the magnetic suction to be primarily supplied by the PMs and RMs. In general, for the coupling problem of thermal, magnetic, and stress fields, this is predominantly rooted in the temperature-induced variations in the magnetic materials' properties. These fluctuations modify the EPM's magnetic capabilities, subsequently altering the magnetic attraction between the suction plate and the EPM pad, and thus influencing the blank holder force.

The magnetic performance parameters of PMs and RMs measured at various temperatures were imported into the magnetic field simulation model in Maxwell software (2022 R1) for simulation. A magnetic flux density contour map was then obtained for the surface of the suction plate and the contact surface of the EPM magnetic pad. As shown in Figure 7a–c, the magnetic flux density on the surface of the attracted plate gradually weakens with the rising temperature, which signifies a reduction in the magnetic flux lines passing through the suction plate. A marker line is drawn on the contour map, and the specific values of magnetic flux density are recorded, as demonstrated in Figure 7d, indicating a decrease in magnetic induction strength with increasing temperature.

According to previous research [23], when structural parameters are fixed, the magnetic attraction force is solely related to the surface magnetization intensity of the attracted plate and is positively correlated with it. The force experienced by the attracted plate under the magnetic force model with different temperature-dependent magnetic performance

parameters has been simulated and calculated, with the results shown in Figure 7e. The magnetic force of FMPUs on the suction plate is 16.524 KN at 25 °C. When the temperature rises to 50 °C, the magnetic attractive force decreases to 15.6195 KN, a drop of 0.9045 KN or 5.474%. When the temperature rises further to 75 °C, the magnetic attractive force drops further to 13.455 KN, a drop of 3.069 KN or 18.57%.

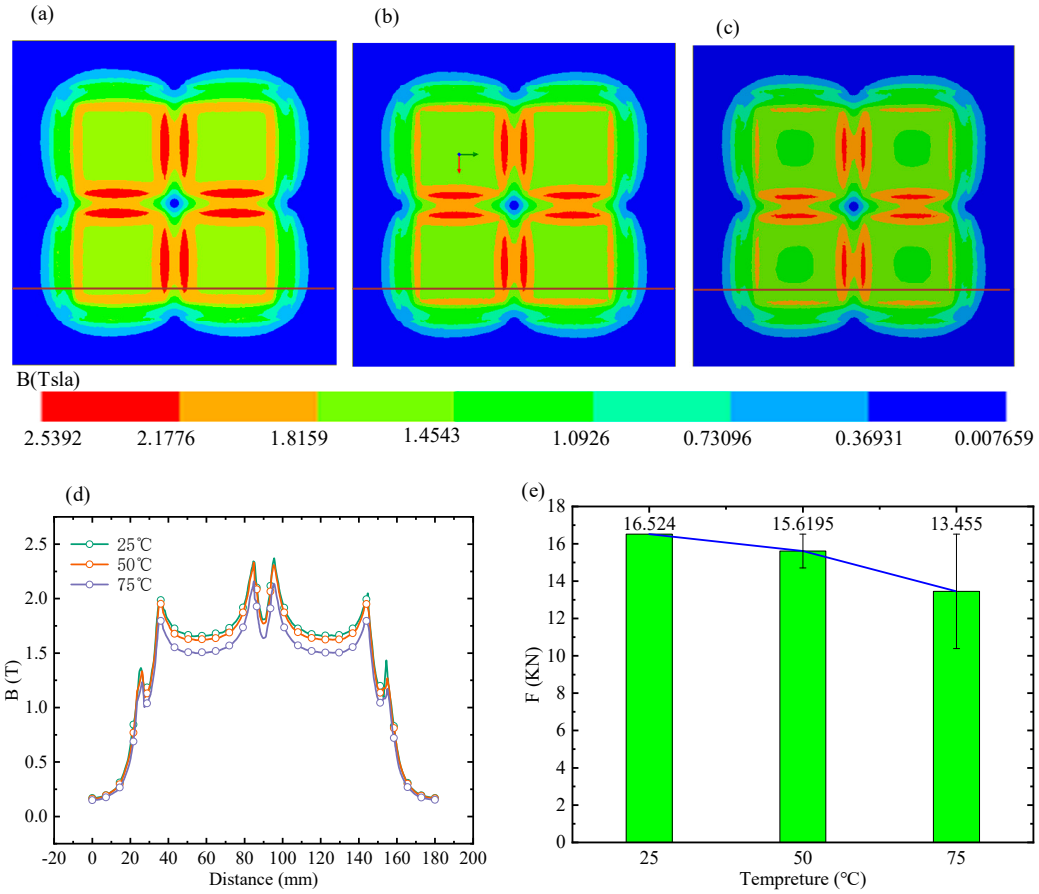


Figure 7. The analysis results of coupling thermal, magnetic, and stress fields under loading conditions: magnetic induction intensity contour maps of the attracted plate surface at different temperatures ((**a**) 25 °C, (**b**) 50 °C, (**c**) 75 °C); (**d**) magnetic induction intensity curve recorded by the marking line; (**e**) magnetic force variation curve graph at different temperatures.

Using the same method for the finite element analysis of the unloaded state of FMPUs, as shown in Figure 8a–c. the distribution of magnetic induction lines at 25 °C, 50 °C, and 75 °C under the condition of magnetic unloading, As shown in Figure 8d, the magnetic force changes at different temperatures. At 25 °C, the residual magnetic attraction force of the attracted plate is 102.3 N, with a corresponding unload ratio of 0.6%. At 50 °C, the residual magnetic attraction force increases to 110.6 N, and the unload ratio slightly rises to 0.7%. At 75 °C, the residual magnetic attraction force further increases to 125.4 N, with an unload ratio of 0.93%. This indicates that as the temperature rises, the residual magnetic attraction force does indeed increase, but the unload ratio consistently remains below 1%, suggesting that the temperature increase has a minimal effect on the unloading of the magnetic device.

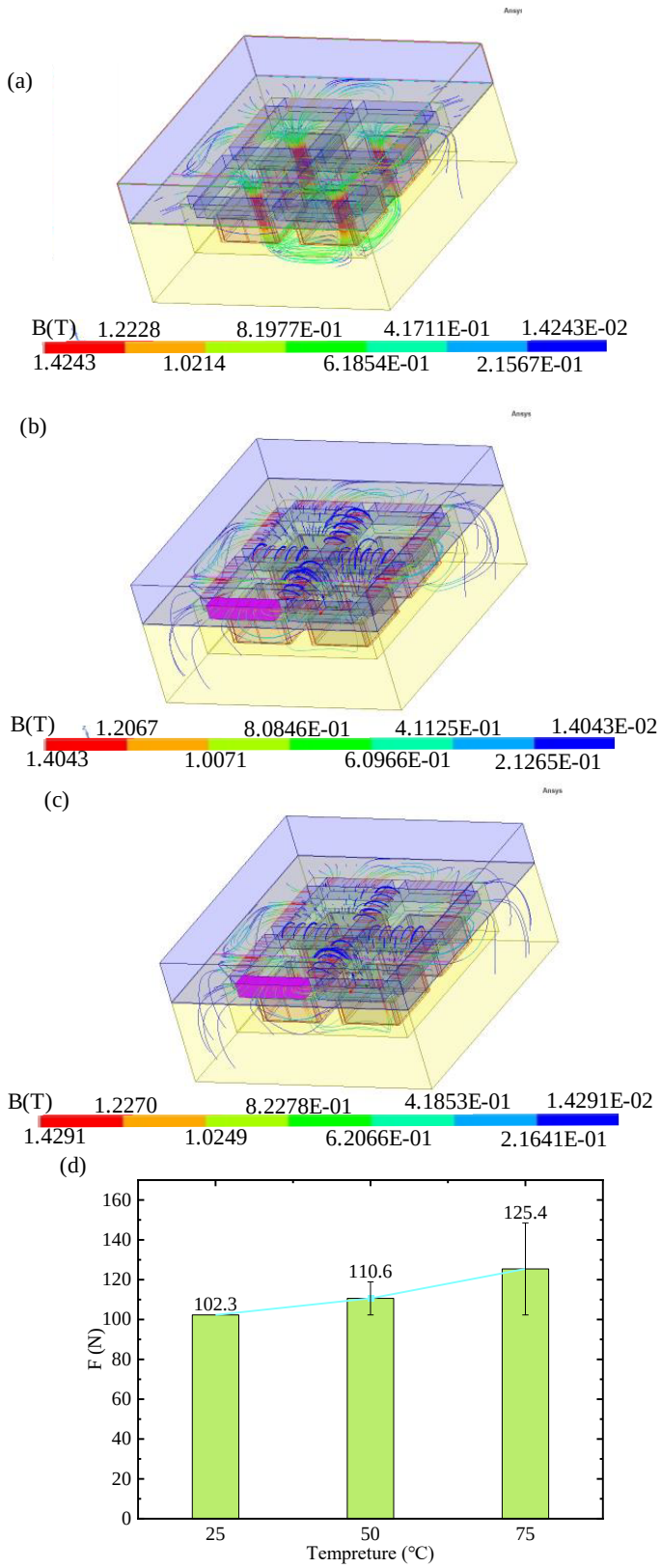


Figure 8. The analysis results of coupling thermal, magnetic, and stress fields under unloading conditions: distribution of magnetic induction lines at different temperatures ((**a**) 25 °C, (**b**) 50 °C, (**c**) 75 °C); (**d**) residual magnetic force at different temperatures.

3. Results

3.1. Experimental Verification

As shown in Figure 9a, the threaded force sensor is fixed to the back of the suction plate using a bolt, a through-hole is set in the middle of the suction plate, and the force-transmitting copper pillar passes through the hole to make contact with the FMPUs. A positive current is applied to the EPM by the EMP controller, generating a magnetic attraction force from the suction cup. This magnetic force is transferred to the force sensor through the force-transmitting copper pillar. During the experiment, the magnetizing and demagnetizing currents as well as their frequencies are set according to the designed operating parameters of the suction cup. The experiment is conducted, and during the process, signals from the temperature sensor and force sensor are conditioned by signal conditioners. The measurement and control system collects sensor signals through an acquisition card and carries out data storage and display. The experimental apparatus is shown in Figure 9b.

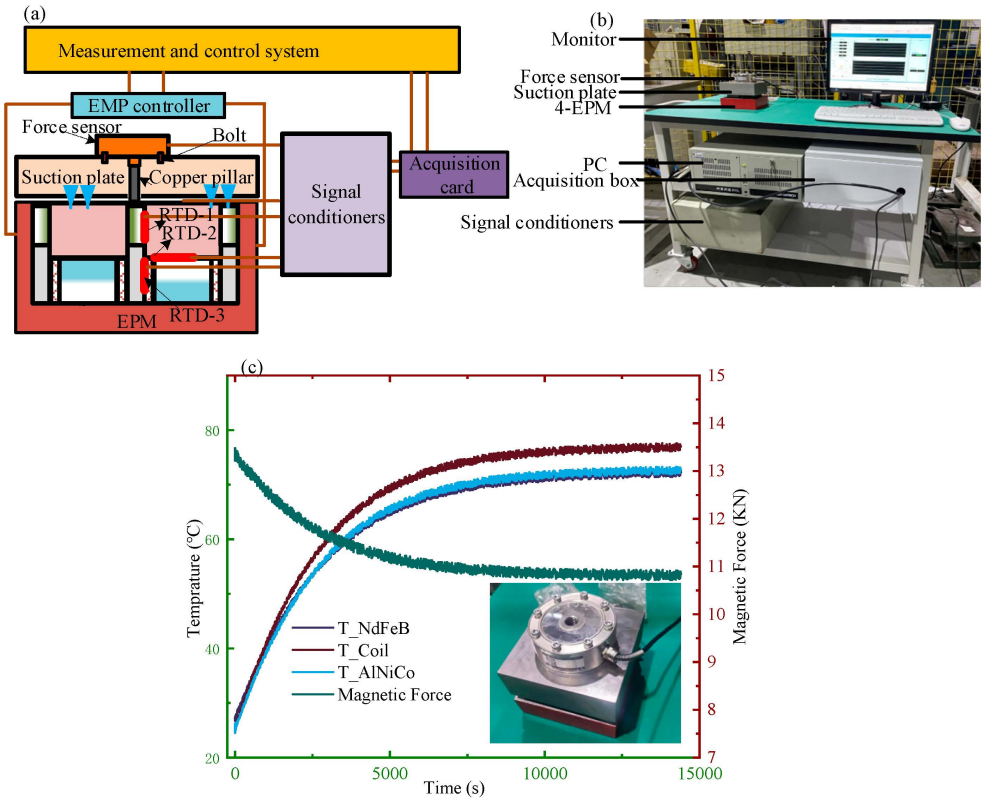


Figure 9. Temperature–magnetic force test apparatus: (**a**) the schematic of the device; (**b**) photo of experimental apparatus; (**c**) results of experiment.

The error between the simulated data and the experimental data is represented by %E, and its calculation formula is shown in Equation (9); in Equation (9), $\hat{y}_i$ represents the simulated value and y_i represents the measured value.

$$\%E = \frac{\left| y_i - \hat{y}_i \right|}{y_i} * 100\% \tag{9}$$

As shown in Figure 9c, after 4.17 h, each component within the FMPUs magnetic device reached a state of thermal equilibrium. The equilibrium temperature for the PM (NdFeB) was 71.92 °C, and for the RM (AlNiCo), it was 72.82 °C. The temperature error of the PM is 1.09%, and the temperature error of the RM is 0.93%. These temperatures are in

close agreement with the theoretical values listed in Table 2, confirming the accuracy of the thermal network model for calculating the temperatures of the components within the magnetic device.

As the temperature increased, the magnetic attraction force gradually weakened, decreasing from an initial 13.22 KN to 10.18 KN, a decline of 22.99%. Compared to the simulated values, the simulation errors for the initial and final values of magnetic force are 22.81% and 25.76%, respectively. This is due to a certain magnetic gap during the experimental measurements, which caused some loss of magnetic force. The magnitude of magnetic force attenuation is approximately similar, with a difference of 4.425%. This consistency validates the precision of the finite element analysis of the coupled thermal–magnetic force field in the EPM magnetic pad.

3.2. Deep Drawing Process Based on EPMBH

The deep drawing equipment is shown in Figure 10. To assess the impact of magnetic force reduction due to temperature rise on the forming effect, this study conducted stretching experiments on 08AL (60 mm in radius and 0.6 mm thick) steel plates under four different edge pressing force conditions, the initial edge pressing forces were set at 55 KN and 42 KN, and the corresponding forces after an 18% reduction were 45 KN and 34 KN.

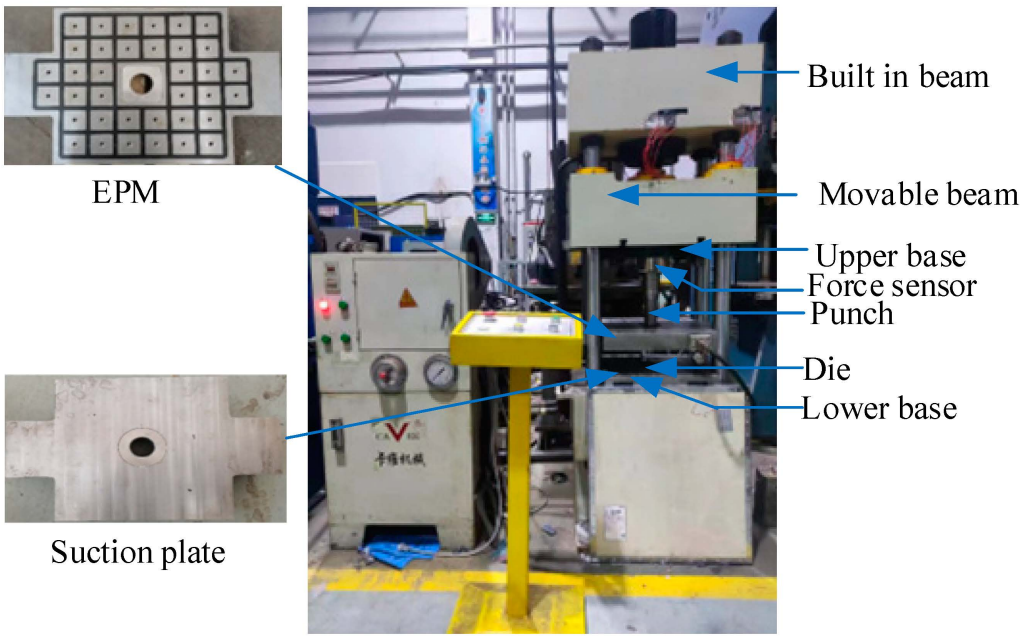


Figure 10. Photograph of experimental setup.

The experimental results, shown in Figure 11, indicate that with an initial edge pressing force of 55 KN, the forming effect on the steel plate was good; even when the force was decreased to 45 KN, the forming quality remained satisfactory. However, with an initial force of 42 KN, while the forming effect appeared to be good at first, wrinkling occurred in the flange area of the plate when the force was reduced to 32 KN, indicating that the edge pressing force was insufficient to complete the deep drawing forming. Therefore, during the EPMBH deep drawing process, it is crucial to pay attention to the reduction in magnetic force caused by temperature rise and to select an appropriate edge pressing force to ensure the effective progression of the forming process.

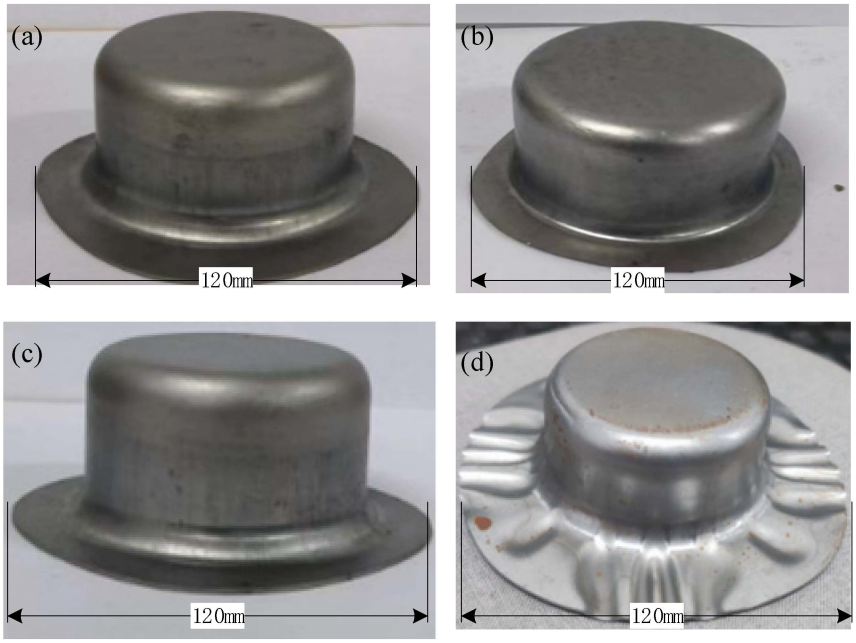


Figure 11. Drawn cups of 08Al sheet with diameter of 60 mm: (**a**) forming effect with BHF of 55 KN; (**b**) forming effect with BHF of 45 KN; (**c**) forming effect with BHF of 42 KN; (**d**) forming effect with BHF of 34 KN.

4. Comparative Analysis of Energy Consumption

The EPMBH process uses the magnetic force of permanent magnets as the blank holder force, significantly reducing energy consumption. To demonstrate the energy-saving effect of this process, an analysis of the process energy consumption was conducted with the target blank holder forces set at 42 kN and 153 kN, respectively.

The energy consumption of the EPMBH process is primarily due to the heat generated by the excitation current passing through the excitation coil. The energy consumption Q for a complete deep drawing process is shown in Equation (10).

$$Q = \left(I_m^2 + I_d^2\right) * R * T_{ct} \tag{10}$$

I_m and I_d are the loading and unloading currents, respectively. R is the resistance of the control coil, 180 Ω. T_{ct} is the working time of the loading current and unloading current, 0.02 s., with the target BHF being 42 kN and 153 kN. In the EPM blank holder process, the loading current I_{m42} is 8 A and I_{m153} is 15 A; the unloading current under different loading currents is the same as 15 A.

According to the previous study [25], in the traditional BHF deep drawing process, the energy consumptions of 42 kN and 153 kN BHF in a deep drawing cycle are 1.89 kJ and 6.89 kJ, respectively.

Figure 12 presents the energy consumption comparison using different blank holder techniques. In comparison to a traditional deep drawing process, the EPMBH process is more energy-efficient than the conventional hydraulic blank holder deep drawing process. When the target blank holder force is 42 kN, it achieves a 44.97% energy saving compared to the traditional hydraulic process. At a target blank holder force of 153 kN, the energy savings increase to 76.48%. This indicates that the greater the target blank holder force, the more significant the energy-saving effect.

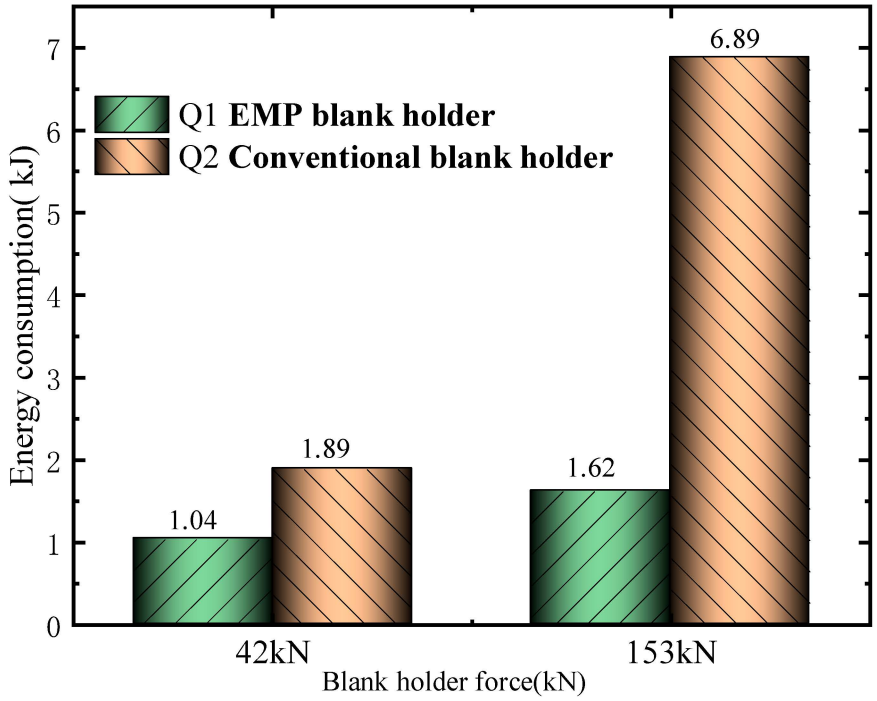


Figure 12. Comparison of energy consumption.

5. Discussion

The electric control permanent magnet technology converts magnetic force into edge pressing force, offering significant energy-saving benefits. Its widespread and long-term application can greatly reduce energy consumption in industrial production, playing a crucial role in promoting carbon neutrality. This paper provides a quantitative analysis of the thermo-magnetic losses in the EPMBH process under conventional conditions, offering data support for its industrial application. According to the experimental results, firstly, a real-time temperature monitoring system for the EPM magnetic device should be established. Secondly, necessary magnetic force compensation should be made based on the temperature–magnetic force variation curve. For scenarios with high performance requirements, high-temperature NdFeB series magnets can be selected, although they are more expensive. Staff can choose suitable permanent magnets based on their specific needs. Future research will focus on reducing thermo-magnetic losses, including analyzing hysteresis losses in high-temperature series permanent magnets, increasing forced convection to lower temperature rise, optimizing load current to reduce heat accumulation, and adding high permeability materials in the working gap to decrease magnetic losses, thereby reducing the operational current and further minimizing heat buildup.

6. Conclusions

Considering the properties of magnetic materials, a finite element analysis of the coupled temperature field–magnetic field–stress field in the EPMBH process was carried out and experimentally verified. The trend of BHF variation with temperature rise in the EPMBH process was deduced and validated through deep drawing tests. Taken together, we can come to the following conclusions:

(1) A thermal network model of the FMPU was constructed using the thermal network analysis method, and calculations were conducted to obtain the thermal equilibrium state of each component. The results indicate that the thermal equilibrium temperature of Alnico (AlNiCo) is 72.12 °C, while that of NdFeB is 72.41 °C; this temperature has not exceeded its curie point, but is close to this critical temperature limit.

(2) The coupling effects of the thermal field, magnetic field, and stress field were analyzed. The results show that as the temperature rises, the magnetic parameters of Alnico (Al-NiCo) remain largely unchanged, whereas those of NdFeB exhibit significant changes, with a maximum magnetic energy product reduction of 17.78%. This reduction leads to a weakened magnetization intensity on the surface of the attracted plate, which in turn reduces the magnetic attraction force on the plate, with a maximum decrease of 18.82%. Therefore, in the application of the EPMBH process, staff need to closely monitor the temperature of the chuck to prevent excessive thermo-magnetic losses.

(3) The deep drawing experiments conducted under the consideration of the temperature rise effect show that the increase in temperature has an impact on the deep drawing process. To successfully complete the deep drawing, it is essential to select the appropriate blank holder force.

Author Contributions: Conceptualization, Z.W. and L.M.; Methodology, L.M.; Software, X.J.; Validation, Z.W.; Formal analysis, L.M.; Investigation, L.M., G.Y. and X.J.; Data curation, Z.W.; Writing—original draft, L.M.; Writing—review and editing, Z.W. and G.Y. All authors have read and agreed to the published version of the manuscript.

Funding: This research received no external funding.

Data Availability Statement: The original contributions presented in the study are included in the article, further inquiries can be directed to the corresponding author.

Conflicts of Interest: Author Xiaoyu Ji was employed by the CCCC Second Harbor Engineering Company Ltd. The remaining authors declare that the research was conducted in the absence of any commercial or financial relationships that could be construed as a potential conflict of interest.

References

1. Tang, H.; Wen, T.; Hong, J.; Zhou, Y.; Zhang, L. Analysis of shear stress wrinkling of asymmetric sheet specimen under offset loading. *J. Mech. Sci. Technol.* **2022**, *36*, 1451–1457. [CrossRef]
2. Siegert, K.; Doegf, E. CNC Hydraulic Multipoint Blank-holder System for Sheet Metal Forming Presses. *CIRP Ann.* **1993**, *42*, 319–322. [CrossRef]
3. Kitayama, S.; Natsume, S.; Yamazaki, K.; Han, J.; Uchida, H. Numerical Investigation and Optimization of Pulsating and Variable Blank Holder Force for Identification of Formability Window for Deep Drawing of Cylindrical Cup. *Int. J. Adv. Manuf. Technol.* **2016**, *82*, 583–593. [CrossRef]
4. Sun, C.Z.; Chen, G.L.; Lin, Z.Q. Improvement of the Formability of Box Deep Drawing Using Variable Force. *J. Shanghai Jiao Tong Univ.* **2003**, *37*, 1883–1886.
5. Du, B.; Zhao, C.; Xie, J.; Li, H.; Zhao, C.; Du, Z. Influence of stress loading path on the limit of plastic wrinkling and instability of plates and shells. *J. Mech. Eng.* **2021**, *57*, 83–91.
6. Bing, D.; Pengfei, S.; Jun, X.; Changcai, Z.; Fenglong, G. Prediction of critical wrinkle instability of thin plates by combining energy method theory with numerical simulation. *J. Mech. Eng.* **2020**, *56*, 57–64. [CrossRef]
7. Won, C.; Kim, H.G.; Lee, S.; Kim, D.; Park, S.; Yoon, J. Wrinkling prediction for GPa-grade steels in sheet metal forming process. *Int. J. Adv. Manuf. Technol.* **2019**, *102*, 3849–3863. [CrossRef]
8. Candra, S.; Batan, I.M.L.; Berata, W.; Pramono, A.S. Analytical study and FEM simulation of the maximum varying blank holder force to prevent cracking on cylindrical cup deep drawing. *Procedia CIRP* **2015**, *26*, 548–553. [CrossRef]
9. Senior, B.W. Flange wrinkling in deep-drawing operations. *J. Mech. Phys. Solids* **1956**, *4*, 235–246. [CrossRef]
10. Hill, R. A theory of the yielding and plastic flow of anisotropic metals. *Proc. R. Soc. London Ser. A Math. Phys. Sci.* **1948**, *193*, 281–297.
11. Hauptmann, M.; Weyhe, J.; Majschak, J.-P. Optimisation of deep drawn paperboard structures by adaptation of the blank holder force trajectory. *J. Mater. Process. Technol.* **2016**, *232*, 142–152. [CrossRef]
12. Sim, H.B.; Boyce, M.C. Finite element analyses of real-time stability control in sheet forming processes. *J. Eng. Mater. Technol.* **1992**, *114*, 180–188. [CrossRef]
13. Kergen, R.; Jodogne, P. *Computerized Control of the Blank Holder Pressure on Deep Drawing Process*; SAE Technical Paper: Warrendale, PA, USA, 1992.
14. Wang, D.Z.; Lou, Z.L.; Zhang, Y.Q. Numerical simulation of variable blank holder force in box deep drawing. *J. Shanghai Jiaotong Univ.* **2001**, *35*, 1543–1546.

15. Cui, X.; Li, J.; Mo, J.; Fang, J.; Zhou, B.; Xiao, X.; Feng, F. Incremental electromagnetic-assisted stamping (IEMAS) with radial magnetic pressure: A novel deep drawing method for forming aluminum alloy sheets. *J. Mater. Process. Technol.* **2016**, *233*, 79–88. [CrossRef]
16. Siopis, M.S.; Kinsey, B.L.; Kota, N.; Ozdoganlar, O.B. Effect of severe prior deformation on electrical-assisted compression of copper specimens. *J. Manuf. Sci. Eng.* **2010**, 731–737. [CrossRef]
17. Fang, J.; Mo, J.; Cui, X.; Li, J.; Zhou, B. Electromagnetic pulse-assisted incremental drawing of aluminum cylindrical cup. *J. Mater. Process. Technol.* **2016**, *238*, 395–408. [CrossRef]
18. Seo, Y.R. Electromagnetic blank restrainer in sheet metal forming processes. *Int. J. Mech. Sci.* **2008**, *50*, 743–751. [CrossRef]
19. Li, H.; Wang, Q.; He, F.; Zheng, Y.; Sun, Y. Design, numerical simulation, and experimental validation of a novel electromagnetic blank holding system for conventional drawing process. *Int. J. Adv. Manuf. Technol.* **2019**, *102*, 2183–2193. [CrossRef]
20. Huang, Y.; Lai, Z.; Cao, Q.; Han, X.; Liu, N.; Li, X.; Chen, M.; Li, L. Controllable pulsed electromagnetic blank holder method for electromagnetic sheet metal forming. *Int. J. Adv. Manuf. Technol.* **2019**, *103*, 4507–4517. [CrossRef]
21. Huang, C.D. Engine with Permanent Magnetic Chucks. US. WO2015021887(A1), 18 February 2015.
22. Cheng, F.; Qin, S.; Lin, Q.; Kong, X. The Electronically Controlled Permanent Magnet Sucker End Pickup for the Rapid Die Changing System of Multi-Station Press: China. CN201020682973.5, 14 December 2010.
23. Qin, S.J.; Zhang, H.S.; Mao, Y.B.; Yang, L.; Li, X.; Hu, Z.; Cheng, X. Electro-permanent magnet blank holder technique in sheet metal deep drawing. *Int. J. Adv. Manuf. Technol.* **2020**, *106*, 5497–5507.D. [CrossRef]
24. Qin, S.; Kong, X.; Ma, Y.; Yang, L. The Invention Relates to a Drawing Die with Variable Blank Holding Force with Memory Characteristics and a Control Method: China. Patent 201610606036.3, 14 December 2016.
25. Zhang, H.; Qin, S.; Cao, L.; Meng, L. Research on Deep Drawing Process Using Radial Segmental Blank Holder based on Electro-permanent Magnet Technology. *J. Manuf. Process.* **2020**, *59*, 636–648. [CrossRef]
26. Qin, S.; Cheng, X.; Zhang, H.; Lu, T.; Gu, T.; Meng, L. Analyses of thermal field and coupled magnetic-mechanical field in electro-permanent magnet blank holder technique. *Int. J. Adv. Manuf. Technol.* **2020**, *110*, 499–510. [CrossRef]
27. Li, Y.; Li, H.; Geng, H.; Gong, X.; Yang, F. Measurement and Analysis of Hysteresis Loss of Nd-Fe-B Permanent Magnet under Superheated Loss of Magnetism. *Electr. Power* **2020**, *50*, 50–57.

Disclaimer/Publisher's Note: The statements, opinions and data contained in all publications are solely those of the individual author(s) and contributor(s) and not of MDPI and/or the editor(s). MDPI and/or the editor(s) disclaim responsibility for any injury to people or property resulting from any ideas, methods, instructions or products referred to in the content.